Crustal Architecture of Puerto Rico Using Body-Wave Seismic Tomography and High-Resolution Earthquake Relocation

Guoqing Lin[*1], Victor A. Huerfano[2], and Wenyuan Fan[3]

Abstract

Puerto Rico is a highly seismically active island, where several damaging historical earthquakes have occurred and frequent small events persist. It situates at the boundary between the Caribbean and North American plates, featuring a complex fault system. Here, we investigate the seismotectonic crustal structure of the island by interpreting the 3D compressional-wave velocity V_P and compressional- to shear-wave velocity ratio V_P/V_S models and by analyzing the distribution of the relocated earthquakes. The 3D velocity models are obtained by applying the simul2000 tomographic inversion algorithm based on the phase arrivals recorded by the Puerto Rico seismic network. We find high-V_P and low-V_P/V_S anomalies in the eastern and central province between the Great Northern Puerto Rico fault zone and the Great Southern Puerto Rico fault zone, correlating with the Utuado pluton. Further, there are low-V_P anomalies beneath both the Great Southern Puerto Rico fault zone and the South Lajas fault, indicating northerly dipping structures from the southwest to the northwest of the island. We relocate 19,095 earthquakes from May 2017 to April 2021 using the new 3D velocity model and waveform cross-correlation data. The relocated seismicity shows trends along the Investigator fault, the Ponce faults, the Guayanilla rift, and the Punta Montalva fault. The majority of the 2019–2021 Southwestern Puerto Rico earthquakes are associated with the Punta Montalva fault. Earthquakes forming 17° northward-dipping structures at various depths possibly manifest continuation of the Muertos trough, along which the Caribbean plate is being subducted beneath the Puerto Rico microplate. Our results show complex fault geometries of a diffuse fault network, suggesting possible subduction process accommodated by faults within a low-velocity zone.

Introduction

Puerto Rico is one of the most densely populated islands in the world with about 3.2 million residents (2019 Census, see Data and Resources). It is of great importance to study the local seismic and tectonic processes to assess seismic hazards and mitigate foreseeable risks from earthquakes. Puerto Rico and the U.S. Virgin Islands (PRVI) are located at the boundary of the North American and the Caribbean plates (small panel in Fig. 1a) and accommodate motions relative to both plates. The North American plate moves west–southwest toward Puerto Rico at a rate of 16.9 ± 1.1 mm/yr (DeMets *et al.*, 2000; Jansma and Mattioli, 2005). The Caribbean plate moves toward the Puerto Rico microplate at a rate of 2.4 mm/yr (Jansma and Mattioli, 2005). The island of Puerto Rico encompasses four seismogenic zones, the Puerto Rico trench in the north, the Muertos trough in the south, the Mona Passage in the west, and the Anegada trough in the east (Fig. 1a, Doser *et al.,* 2005). The relative motion between the subducting North

American plate and the Puerto Rico microplate causes abundant seismicity at the 19° N fault zone south of the Puerto Rico trench (Mccann, 1985; Jansma and Mattioli, 2005). Deformation at the Puerto Rico trench is generally thought to involve both a strike slip and a subduction component, whose tectonics has been examined by previous studies with various means (e.g., McCann and Sykes, 1984; DeMets *et al.,* 2000; Jansma and Mattioli, 2005). However, the Muertos trough south of the island has an enigmatic tectonic history, and whether or not the Caribbean plate subducts beneath Puerto Rico Island has been debated because of inconsistent

1. Department of Marine Geosciences, Rosenstiel School of Marine and Atmospheric Science, University of Miami, Miami, Florida, U.S.A.; 2. Puerto Rico Seismic Network, Geology Department, University of Puerto Rico at Mayagüez, Mayagüez, Puerto Rico, U.S.A.; 3. Institute of Geophysics and Planetary Physics, Scripps Institution of Oceanography, University of California, San Diego, California, U.S.A.

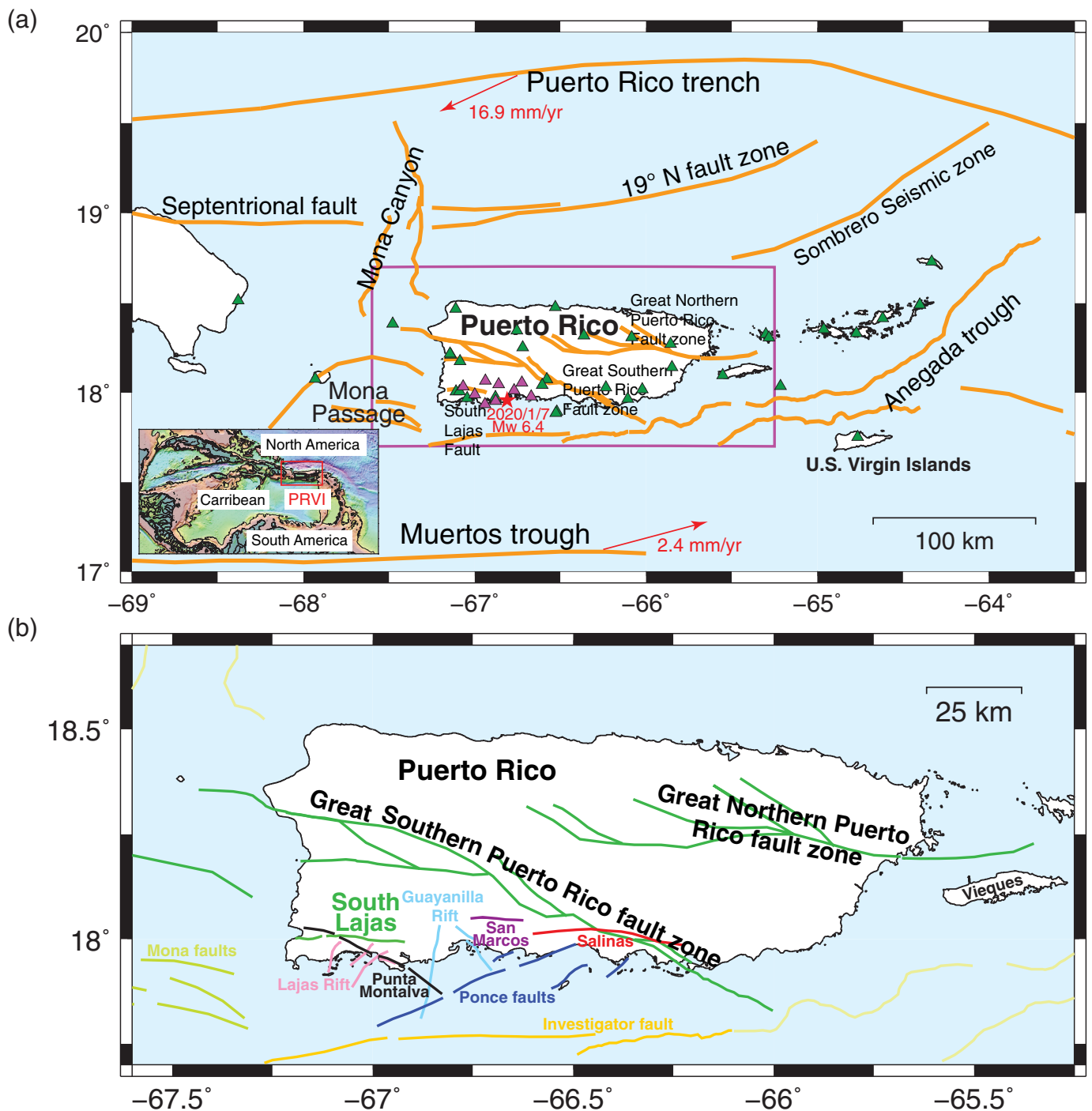*Corresponding author: glin@rsmas.miami.edu

Figure 1. (a) Major geological features in the Puerto Rico and the U.S. Virgin Islands (PRVI) region. Green triangles stand for the permanent Puerto Rico Seismic Network (PRSN) seismic stations and purple ones for those deployed after the 2020 M_w 6.4 earthquake. Major fault zones are denoted by orange lines, including the Great Northern Puerto Rico fault zone, the Great Southern Puerto Rico fault zone, and the South Lajas fault on land. The purple box encloses the focused area of this study (a close-up is shown in b). Two red arrows indicate the plate movement directions relative to the Puerto Rico microplate measured by Global Positioning System data (DeMets et al., 2000; Jansma and Mattioli, 2005). Inset map shows the location of the PRVI region, lying between the North American and the Caribbean plates. Base map of the inset is the topography map compiled by Smith and Sandwell (1997). (b) Detailed fault traces from various sources (Grindlay et al., 2005; Jansma and Mattioli, 2005; Mann et al., 2005; Prentice and Mann, 2005; Addarich-Martínez, 2009; Symithe et al., 2015; Adames-Corraliza, 2017; Piety et al., 2018). The color version of this figure is available only in the electronic edition.
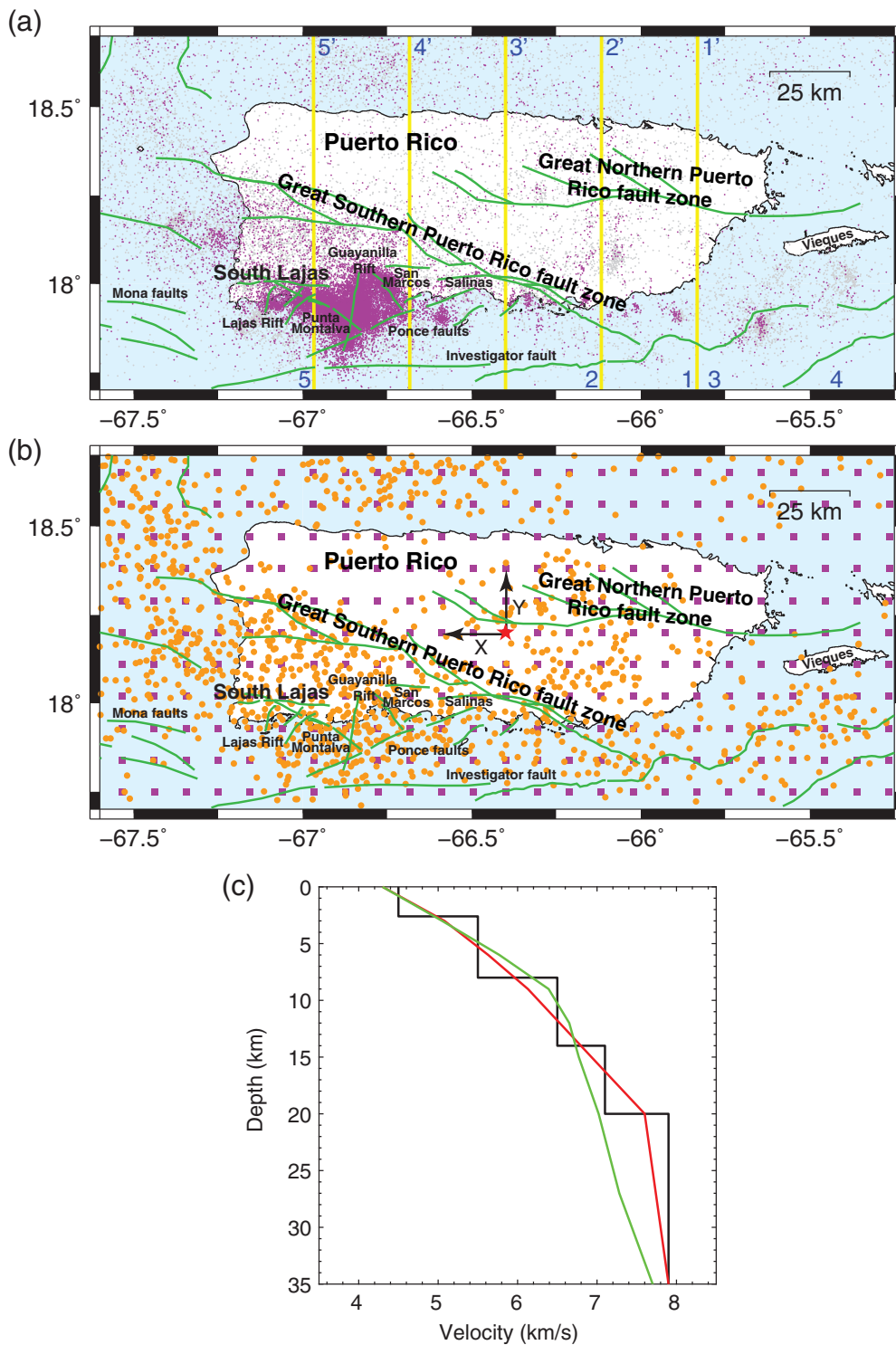
Figure 2. (a) Earthquake distribution (dots) from January 1986 to April 2021 recorded by the PRSN seismic stations. The purple ones represent events from May 2017 to April 2021, which are dominated by the 2019–2021 Southwestern Puerto Rico seismic sequence. The yellow straight lines are the profiles for the cross sections shown in Figure 5. (b) Map view of the master events (orange dots) and grid nodes (purple squares) used in the tomographic inversion. The velocity model is centered at (18.2°, -66.4°) (red star) with the *x* axis pointing to the west direction and *y* axis to the north. (c) 1D V_P models. The black layer-cake one is the model used in the PRSN daily operation. The red one is the initial gradient velocity model derived from the layer-cake model. The green one is the final gradient model used as the starting model for the 3D tomographic inversion. The color version of this figure is available only in the electronic edition.

evidence from seismicity, gravity models, seismic profiles, and bathymetrical data (e.g., Byrne *et al.*, 1985; Bruna *et al.*, 2010).

In addition to the offshore fault systems, the Great Northern Puerto Rico fault zone (GNPRFZ) and the Great Southern Puerto Rico fault zone (GSPRFZ) are the two major inland, strike-slip fault networks, traversing the east and west of the island (Fig. 1b). The South Lajas fault (SLF) in southwest Puerto Rico extends from the southwestern edge of the Lajas Valley, trending along an east–west direction throughout the valley (Fig. 1b, Prentice *et al.*, 2000; Prentice and Mann, 2005). This diffuse and complex tectonic setting makes the Puerto Rico Island a seismically active region.

Every year, thousands of earthquakes occur within and around the Puerto Rico region. At least four destructive earthquakes since 1700 have been documented. Several large earthquakes have been reported in recent history, including the 1916, 1918, and 1943 Mona Passage earthquakes (Doser *et al.*, 2005). The inland seismicity concentrates over the southwestern corner of Puerto Rico (Fig. 2a). Previous studies have shown the underlying serpentinite belts relate to the local tectonic and seismic activity (Grindlay *et al.*, 2005; Huerfano *et al.*, 2005). Smaller faults are often difficult to identify at the surface, probably due to high erosion rate and/or low slip rate (Mccann, 1985). Recently, a previously unknown fault zone, the North Boquerón Bay–Punta Montalva fault zone, was identified and mapped (Fig. 1b) crossing the

Lajas Valley based on detailed analyses of geophysical and geological data (Addarich-Martínez, 2009; Roig-Silva *et al.*, 2013; Adames-Corraliza, 2017). An ongoing seismic sequence (as of August 2021) commenced in this area in December 2019. With its progression into 2021, it had been renamed as the 2019–2021 Southwestern Puerto Rico sequence and is thought to be associated with the Punta Montalva fault zone. This activity has lasted for over 19 months and included more than 15,000 events (by the end of April 2021), with the largest one an M_w 6.4 earthquake on 7 January 2020 (red star in Fig. 1a) south of Indios.

In this study, we invert for 3D compressional-wave velocity (V_P) and compressional- to shear-wave velocity ratio (V_P/V_S) models for the island of Puerto Rico. We also relocate the earthquakes beneath the island using the new velocity model and waveform cross-correlation data. Based on these results, we investigate the seismicity distribution of the 2019–2021 Southwestern Puerto Rico earthquake sequence and the seismotectonic features of the Puerto Rico Island.

Data and Processing

The seismic data used in this study are recorded by the Puerto Rico seismic network (PRSN). PRSN has been monitoring and processing earthquakes in the Puerto Rico region since 1974. It currently consists of four short-period and 30 broadband seismographs (green triangles in Fig. 1a) in Puerto Rico and adjacent islands (Clinton *et al.*, 2006). Additional campaign seismic stations (purple triangles in Fig. 1a) were deployed by PRSN and the U.S. Geological Survey shortly after the M_w 6.4 earthquake in January 2020 and have been operational since then.

The earthquake catalog and phase arrivals of Puerto Rico events are available from PRSN since 1986. For the tomographic inversion in this study, we use the P- and S-wave arrivals for over 34,000 earthquakes (dots in Fig. 2a) from January 1986 to April 2021 in the region. These events are mostly shallower than 30 km depth with most of their magnitudes ranging from 1 to 3.5. To obtain a more uniform event distribution and reduce the computational time for the tomographic inversion, we select a subset of 1222 master events (orange dots in Fig. 2b). These master events have the most picks within 4 km radius with at least eight P and four S arrivals. The average number of first arrivals per event is 13 for P and 12 for S, respectively. Such an event selection procedure has proven effective and efficient in resolving crustal structures in California and Hawai'i (e.g., Lin *et al.*, 2007, 2010, 2014).

For the relocation work, we focus on the 20,724 earthquakes from May 2017 to April 2021 (purple dots in Fig. 2a). In addition to the first P and S arrivals, we download their associated waveforms for all three components (i.e., vertical, east, and north). The data are first resampled to a uniform 100 Hz sample rate and then band-pass filtered between 1 and 10 Hz. The cross correlation is computed for each event with its nearest (up to 200) neighbors within 5 km distance, independently

for P and S waves. We use a 1.5 s window around P wave and a 2.5 s window around S wave when catalog picks are available. If not, we use a 2 s P window and a 3 s S window based on the predicted arrival times using the earthquake location and the 1D initial velocity model used for the tomographic inversion. We only save differential times with the corresponding correlation coefficient (CC) greater than 0.5. Event pairs with less than four satisfying differential times are discarded. This step results in over 96 million differential times for more than 2.6 million event pairs. During the waveform cross-correlation relocation process, we use differential times with CC higher than 0.55 and require each event pair to have at least four differential times with CC higher than 0.6.

Methodology
Tomographic inversion

We implement the simul2000 tomographic algorithm to obtain 3D body-wave velocity models (Thurber, 1983, 1993; Eberhart-Phillips, 1990; Thurber and Eberhart-Phillips, 1999) using the master events. The simul2000 program is a damped least-squares inversion method using the full matrix to simultaneously solve for V_P and V_P/V_S models and earthquake locations. Based on the event and ray distributions, the grid spacing in our final velocity model is selected as 10 km horizontally (purple squares in Fig. 2b) centered at (18.2°, -66.4°) (red star in Fig. 2b) with the x axis pointing to the west direction and y axis to the north. The vertical nodes are positioned at 0, 3, 6, 9, 12, 15, 20, 27, 35, 45, and 60 km depths. All depths in this study are relative to mean sea level.

We perform our 3D tomographic inversion starting from a 1D velocity model. We first create a gradient 1D P-wave velocity model (red solid line in Fig. 2c), based on the 1D layered model used in the PRSN daily operation (black line in Fig. 2c). We choose a constant V_P/V_S ratio of 1.75 derived from the Wadati diagram (Kisslinger and Engdahl, 1973), which is consistent with the average values in the nearby Caribbean regions (e.g., Corbeau *et al.*, 2017; Kumar *et al.*, 2020; Londoño *et al.*, 2020). Next, we start with the gradient V_P model and the constant V_P/V_S ratio to run the tomographic inversion. The layer-averaged values of the output models are set as the 1D starting models for the next round of inversion. This iterative process is repeated until the input and output velocity models converge with marginal differences and equal data fits. In our case, the difference in the sum of squared residuals resulted from the two models is smaller than 0.1%. The average values of the V_P/V_S ratios at different layers remain at 1.75 during these iterations and thus are used in all the inversions. The input model used in the final 3D tomographic inversion is shown by the green line in Figure 2c. This iterative procedure helps to resolve a model that best represents the average value at each depth layer with minimal velocity perturbations. The well-resolved velocity structures in the final model show no significant dependence on the initial 1D model.
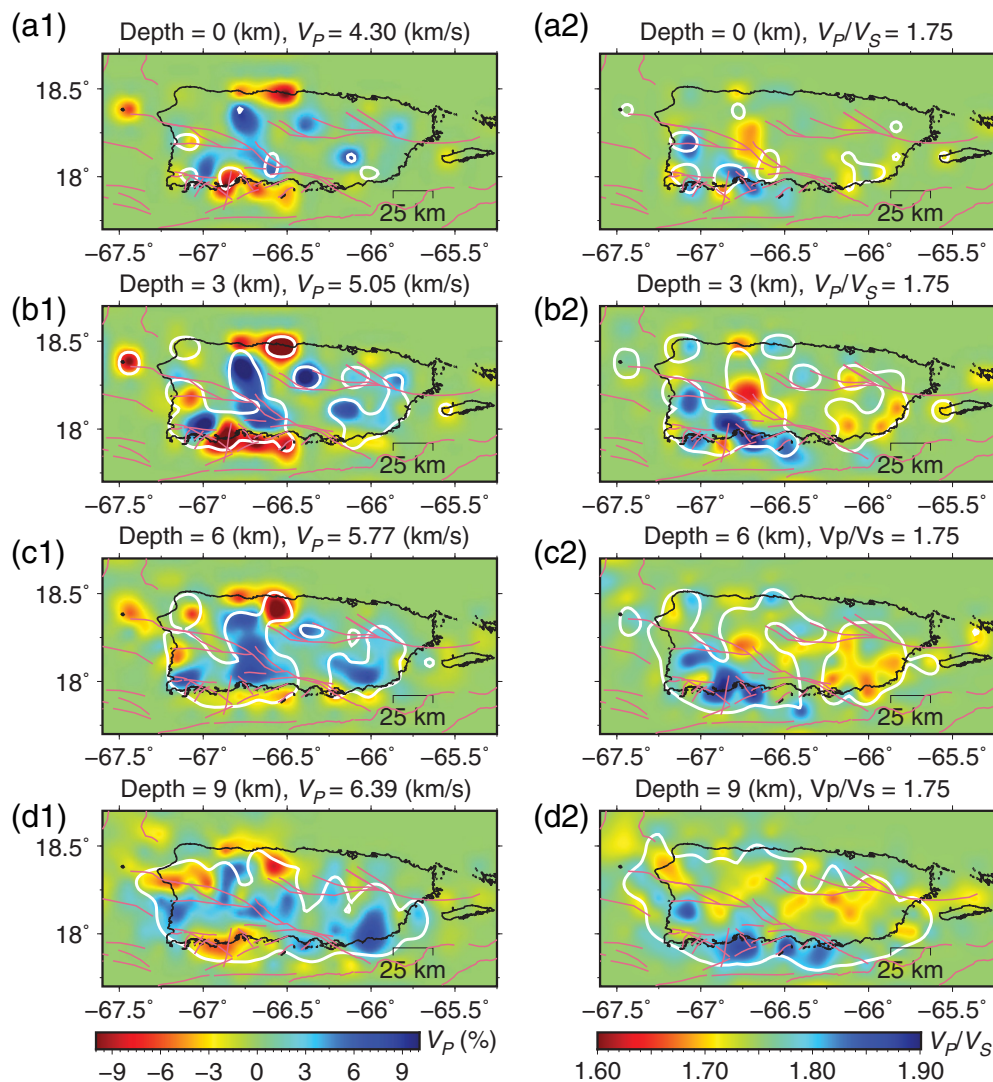
Figure 3. Map views of the final 3D (a1–d1) V_P and (a2–d2) V_P/V_S models at four depth slices from 0 to 9 km depth for the study area. V_P perturbations are shown relative to the slice-average values, shown at the top of each subfigure. White contours enclose areas with the resolution matrix diagonal element (RDE) value greater than 0.1. Pink lines represent the fault traces. The color version of this figure is available only in the electronic edition.

to invert the 3D V_P and V_P/V_S models. The comparison of the true and inverted models is shown in the supplemental material available to this article. The models are generally well recovered from 6 to 27 km depths, and the southwestern portion of the island has the best model resolution. Based on the recovered patterns, we use RDE ≥ 0.1 as a confidence interval to contour the well-resolved regions and focus our discussions on the features within these areas. We note that the model resolution could be significantly increased if smaller damping values were used. However, we prefer relatively larger damping parameters in this study to retrieve the most reliable velocity structures.

Earthquake relocation

Three-dimensional velocity models of crustal and upper mantle structures can greatly improve absolute hypocentral locations by correcting the biasing effects from large-scale velocity variations. We use our newly developed 3D velocity model to relocate all the seismicity from May 2017 to April 2021 beneath and near the island of Puerto Rico. During the inve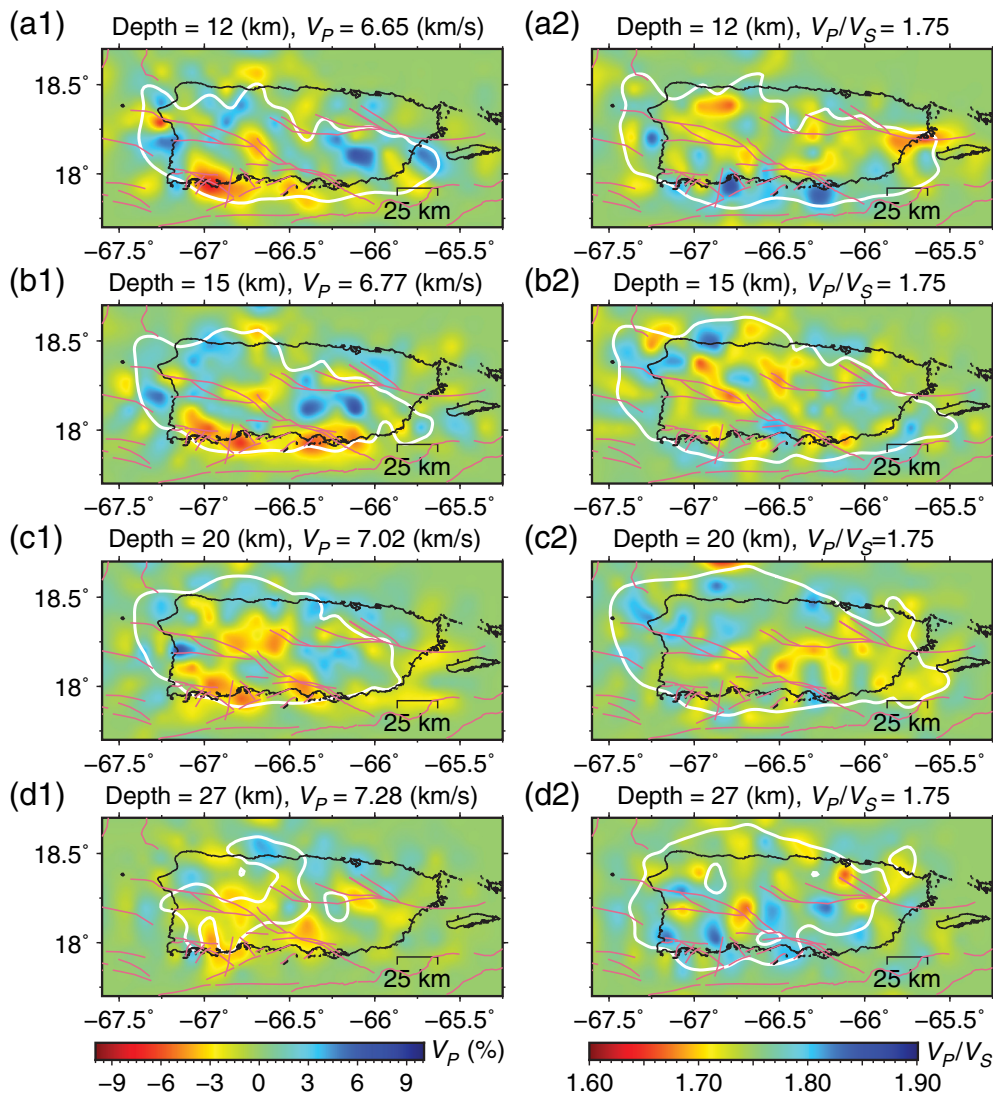rsion, we keep the V_P and V_P/V_S models fixed and only allow the earthquake hypocenters to vary for a few iterations until convergence. We refer to the relocation result after this step as the 3D location. The absolute location uncertainties are computed by the tomographic algorithm for both horizontal and vertical directions.

Because simul2000 is a damped least-squares method, the optimal damping parameters used in our inversion are selected by compromising the data and model variances (e.g., Eberhart-Phillips, 1986, 1993). During the tomographic inversion, the simul2000 algorithm also computes the resolution matrix, whose diagonal element (RDE) can serve as an assessment for model recovery. To further examine the model resolution, we perform checkerboard tests to evaluate the inversion parameters and the recovery capability of the data. We construct checkerboard patterns with every 20 km gridding along both x and y directions and velocity perturbations of ± 5% relative to the layer-averaged values of the 1D initial model. Using the synthetic travel times calculated from the perturbed velocity model, we apply the same parameterization as for the real data

Starting with the 3D locations, we further improve relative earthquake locations by applying a differential time location technique (Lin, 2018) based on waveform cross-correlation data. The approach has proved successful in relocating large sets of earthquakes in California and Hawai'i (e.g., Lin et al., 2007, 2014; Lin and Okubo, 2016, 2020). This method solves for the location of each earthquake that minimizes the differential time residuals between the target event and the linked events in the study area. The relative horizontal and vertical

Figure 4. Map views of the final 3D (a1–d1) V_P and (a2–d2) V_P/V_S models at four depth slices from 12 to 27 km depth for the study area. Symbols are the same as those in Figure 3. The color version of this figure is available only in the electronic edition.

the comparable numbers of P and S picks used in the inversion, the V_P and V_P/V_S models have similar resolutions and the models are presented side by side from 0 to 27 km depth in Figures 3 and 4. Although resolutions of the V_P and V_P/V_S models are limited at 0 km depth slice, our velocity structures at shallow depths show general correlations with the surface geology (e.g., Schellekens, 1998; Huerfano et al., 2005). From 0 to 9 km depth (Fig. 3), multiple prominent anomalous features are shown near the north central coast, the central province between the GNPRFZ and the GSPRFZ, and the southwest of the island. Near the north central coast, we observe very low V_P (up to −10% relative to the average value) and slightly high-V_P/V_S anomalies, which may correlate with the North Coast Tertiary basin of Puerto Rico, at the boundary zone between the North American and Caribbean plates (Larue et al., 1998; Mendoza and McCann, 2009). In between the GNPRFZ and the GSPRFZ, the central and eastern island region has high-V_P values and low-V_P/V_S ratios. In particular, the shape of the resolved structures in the eastern island and south of the GNPRFZ is consistent with the San Lorenzo batholiths (Huerfano et al., 2005). The highest V_P-value occurs near the central GSPRFZ, extending to the north–northwest direction, probably associated with the Utuado pluton (Jolly et al., 1998; Huerfano et al., 2005). Similar to the north central coast, the south coast basin is imaged with low-V_P and high-V_P/V_S anomalies with stronger perturbations relative to the slice average values, coinciding with the sedimentary rocks in the area (Schellekens, 1998). Most of these structural anomalies extend deep into the mid- and lower crust from 12 to 27 km depth, but with subdued amplitudes (Fig. 4). However, the high-V_P and low-V_P/V_S bodies between the GNPRFZ and the GSPRFZ gradually reverse into low-V_P and high-V_P/V_S anomalies from 12 to 27 km depth. The reversal of the velocity

location uncertainties are estimated by bootstrapping (Efron and Tibshirani, 1991) the differential times of each earthquake.

It has been found that differential times between large earthquakes and smaller events may lead to unreliable locations for large events (Bachura and Fischer, 2019) because of their complex waveforms, high amplitudes, and frequently clipping the records. Therefore, we exclude $M \geq 5$ events in the waveform cross-correlation relocation process and present the 2020 M_w 6.4 earthquake at its 3D location for reference.
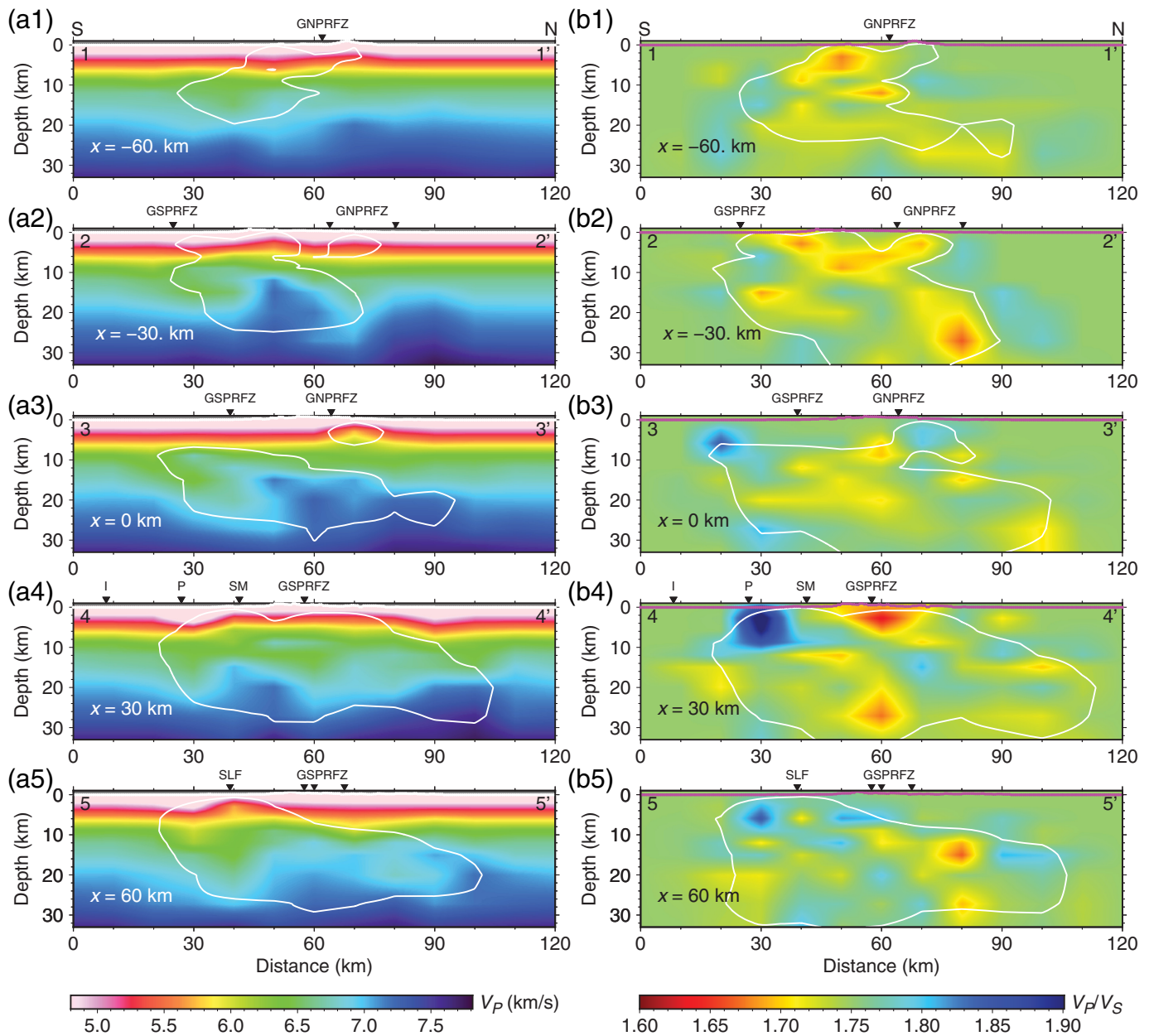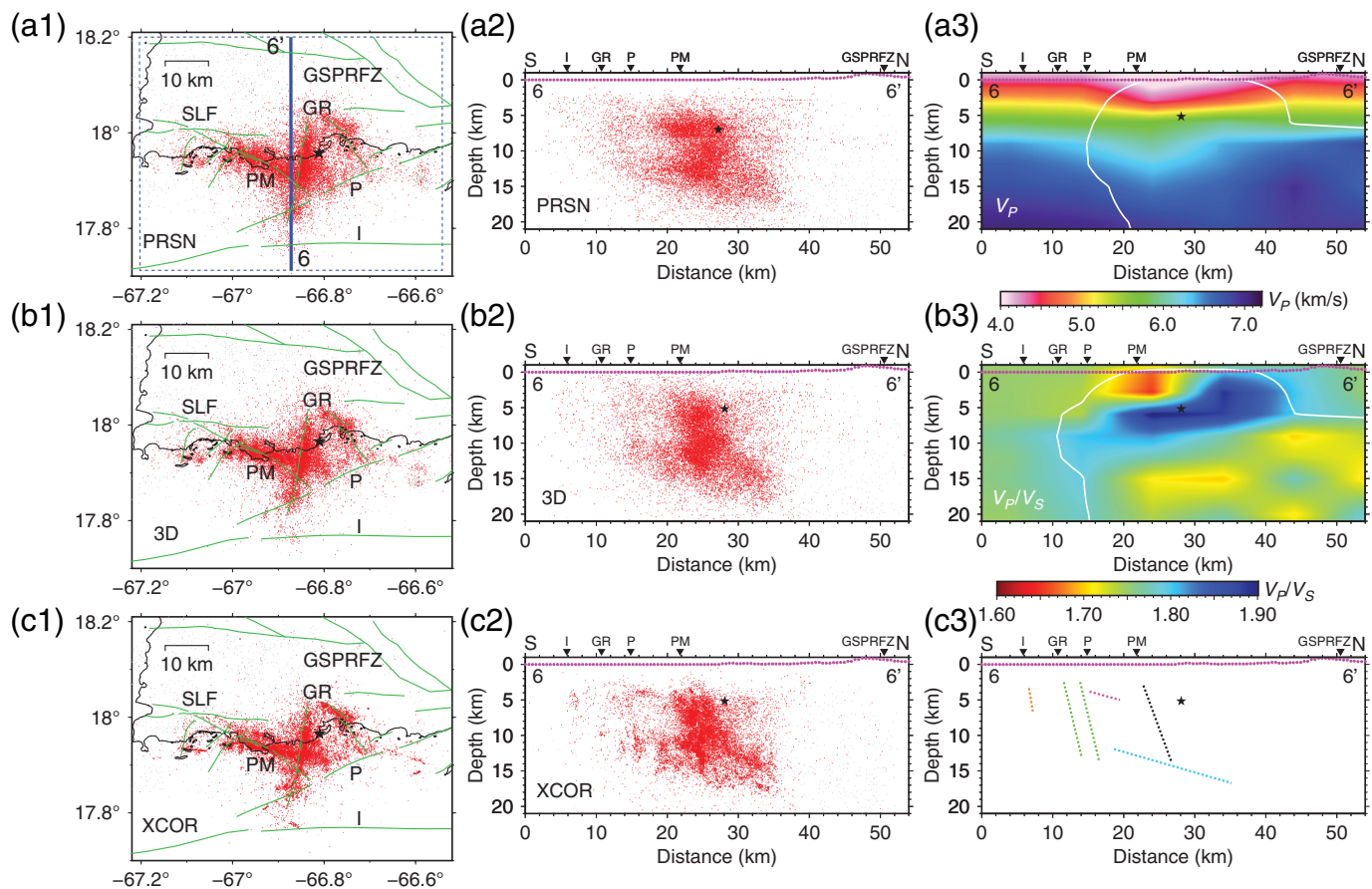
Results and Discussions
Final V_P and V_P/V_S models
After the final tomographic inversion, the median absolute deviation of arrival-time residuals was dropped from 0.34 to 0.09 s for P and from 0.37 to 0.11 s for S wave. Because of

Figure 5. Depth distribution of the final 3D (a1–a5) V_P and (b1–b5) V_P/V_S models along five south–north profiles (1–1′ to 5–5′) migrating from the east to the west of the island. Profile locations are shown by the yellow vertical lines in Figure 2a. White contours enclose areas with the RDE value greater than 0.1. GNPRFZ, Great Northern Puerto Rico fault zone; GSPRFZ, Great Southern Puerto Rico fault zone; I, Investigator fault; P, Ponce faults; SM, San Marcos fault; SLF, South Lajas fault. The color version of this figure is available only in the electronic edition.

anomalies may be related to the isostatic response for the density anomalies within these mountainous regions and warrant further investigation with integration of other geophysical data.

In Figure 5, we show five vertical profiles of the absolute V_P and V_P/V_S models along the south–north direction moving from the east to the west of the island. Along the easternmost profile 1–1′, the V_P model is only well resolved in the central area above 20 km depth, with slightly low-V_P value. The V_P/V_S ratios are generally low (≤1.7) within the resolution contour. Along profiles 2–2′ and 3–3′, the high-V_P body at 10–20 km depths between the GNPRFZ and the GSPRFZ is prominent, which is one of the best-resolved features in our V_P velocity model. The V_P/V_S model shows different patterns from each other along these two profiles. Along the profile 2–2′, there seems to be a north-dipping high-V_P/V_S zone corresponding

to the high-V_P zone, surrounded by multiple very low-V_P/V_S anomalies. In contrast, along profile 3–3′, the V_P/V_S model shows relatively low values corresponding to the high-V_P body. Along profile 4–4′, although the V_P still shows high values between the GNPRFZ and the GSPRFZ, the most visible

Figure 6. Comparison of different location catalogs in the adjacent area of the 2019–2021 seismic sequence. (a1) Map view of the PRSN location, (a2) depth distribution of the PRSN location, (b1) map view of the 3D location, (b2) depth distribution of the 3D location, (c1) map view of the cross-correlation location, and (c2) depth distribution of the cross-correlation location. Gray dots stand for the earthquakes before 28 December 2019, and red for those on or after that. Depth distributions (middle column) are plotted for the seismicity along profile 6–6′ (thick blue straight line) and within the dotted box in (a1). Stars in (a1) and (a2) show the PRSN location of the 2020 M_{w} 6.4 earthquake, and those in other subfigures are the 3D relocation of the earthquake from this study. (a3) V_P model along profile 6–6′. White contours enclose areas with the RDE value greater than 0.1. (b3) V_P/V_S model along profile 6–6′. White contours enclose areas with the RDE value greater than 0.1. (c3) Lines highlighting the seismicity trends in (c2) that are discussed in the Relocation Results section. GR, Guayanilla rift; GSPRFZ, Great Southern Puerto Rico fault zone; I, Investigator fault; P, Ponce faults; PM, Punta Montalva fault and its extension; SLF, South Lajas fault. Note that the same number of earthquakes are plotted in each location catalog. The color version of this figure is available only in the electronic edition.

anomaly is in the south of the GSPRFZ. The V_P/V_S model along this profile shows a complex pattern with both the lowest and highest values among these five profiles. The high V_P/V_S occurs in the south coast (from 24 to 36 km distance), extending to about 8 km depth, and collocates with a low-V_P zone in the same area. A low-V_P/V_S body takes place beneath the GSPRFZ (∼60 km distance) from the surface to about 8 km depth. Below it, a north-dipping high-V_P/V_S feature extends from 5 km depth beneath the San Marcos fault to ∼25 km depth north of the GSPRFZ. A second low-V_P/V_S body beneath the GSPRFZ stretches from 15 down to 30 km depth. The corresponding V_P model of this area shows low values at shallow (<8 km) and deep (>15 km) depths and a thin high-V_P body centered at about 10 km depth. The velocity model along profile 5–5′ displays distinct features, including very low-V_P values beneath the South Lajas fault (from 32 to 50 km distance) from the surface to 30 km depth and a low-V_P structure (from 50 to 92 km distance) dipping northward throughout the island, which could reflect the Caribbean slab subducting beneath Puerto Rico. The V_P/V_S ratios outline a similar dipping structure with low values with intermittent high-V_P/V_S bodies along the dipping trend.

Relocation results

For all the 20,154 earthquakes relocated by the 3D velocity model, the absolute locations have median uncertainties of

103 and 122 m in the horizontal and vertical directions, respectively. In Figure 6a1,a2 and b1,b2, we compare these 3D locations with the PRSN network catalog in the region near the 2019–2021 seismic sequence. There are significant differences in the absolute location and marginal ones in seismicity spatial

spread. For example, the 3D relocated earthquakes south of the 2020 M_w 6.4 mainshock location (Fig. b2) form a more steeply dipping feature than in the PRSN catalog (Fig. a2).

We further relocate 19,095 earthquakes (95% of the input 3D relocated events) with the waveform cross-correlation method to investigate the detailed fault structures of the area. Our results have median relative location uncertainties of 69 and 64 m in the horizontal and vertical directions, respectively. These waveform cross-correlation relocations are compared along the same profile with the 3D and the PRSN locations in Figure 6. Further location comparisons along a west–east profile are shown in the supplemental material. We obtain a more compact earthquake distribution from the waveform cross-correlation results, although the relocation does not produce dramatic sharpenings delineating fault traces that are often observed in California or Hawai'i after similar procedures (e.g., Lin *et al.*, 2007, 2014; Lin and Okubo, 2016, 2020). This wide spatial spread is likely real, which may reflect the complex tectonic setting in Puerto Rico causing intertwined fault networks.

Despite the spread of the earthquakes, our relocation results show trends that may correlate with the surface traces of multiple active faults identified from geological surveys (Fig. 6c2). For example, a near-vertical seismicity streak located at 6.8 km distance and ~5 km depth (highlighted by the orange dotted line in Fig. 6c3) is coincident with the projection of the Investigator fault (LaForge *et al.*, 2005). Farther north, the seismicity beneath the southernmost segment of the Guayanilla rift and the Ponce faults shows steep north-dipping trends (highlighted by the green dotted lines in Fig. 6c3), whose surface extensions agree well with the mapped fault lines. Near the Punta Montalva, where most of the earthquakes occur, there appears to be two linear trends. The steep linear trend (highlighted by the black dotted line in Fig. 6c3) has a dipping angle of ~71° and extends to the Punta Montalva fault at the surface. The other gentle trend (highlighted by the blue dotted line in Fig. 6c3) has a lower dipping angle of ~17°, which nicely agrees with the inferred dip angle for the Muertos subduction zone based on the study of a 1984 M_s 6.7 thrust event in the area (Byrne *et al.*, 1985; LaForge *et al.*, 2005). At 4 km depth between the Ponce faults and the Punta Montalva fault, there is a small cluster of events parallel to the 17° dipping linearity (highlighted by the pink dotted line in Fig. 6c3). These results suggest that a complex fault network with multiple fault planes dipping from gentle to steep toward the north direction may have been active during the 2019–2021 earthquake sequence.

Intriguingly, the seismicity patterns do not directly correlate with the structure features of the V_P and V_P/V_S models along the profile. The V_P model is dominated by the low-velocity body south of the GSPRFZ (Fig. 6a3), most obvious in the region south of the 2020 M_w 6.4 mainshock. There is a strong high-value, south-dipping feature in the V_P/V_S model (Fig. 6b3), originating from the surface in the GSPRFZ and extending southward to

~10 km depth beneath the southern end of the Guayanilla rift. The high-V_P/V_S anomaly smears to greater depths, but this is probably due to the limited resolution in this area. Below this anomalous feature, there are scattered low-V_P/V_S patches in between the GSPRFZ and the Punta Montalva fault. Above this high anomaly, there is a low-V_P/V_S zone beneath the Punta Montalva fault above 4 km depth, which spatially compacts with a horizontal extent of 10 km.

2019–2021 Southwestern Puerto Rico sequence

The 2019–2021 Southwestern Puerto Rico sequence has lasted over 19 months (as of August 2021) and consists of most of the relocated earthquakes. About 83% of the waveform cross-correlation relocations occurred after the initiation of the seismic sequence on 28 December 2019. The daily seismicity rate from May 2017 to April 2021 shows abrupt increases in December 2019 and January 2021 (see supplemental material). The 2019–2021 Southwestern Puerto Rico sequence has been associated with the Punta Montalva fault (e.g., López Venegas *et al.*, 2020). The map view of our relocations (Fig. 6c1) seems to suggest that the sequence is bounded by the Investigator fault and Ponce faults in the southern and eastern ends and extends along the Punta Montalva fault and the Guayanilla rift. The depth distribution of the earthquakes (Fig. 6c2) indicates that all these nearby faults are active with most of the earthquakes occurring near the Punta Montalva fault. The 2020 M_w 6.4 mainshock is relocated at the edge of the seismicity zone beneath the Punta Montalva fault and near the boundary between the dominant high- and low-V_P/V_S bodies (Fig. 6b3), which may suggest variations of material properties or fluid contents in the area.

Implications

Whether there is an active subduction from the Caribbean plate beneath the Puerto Rico Island has important implication in regional tectonics and seismogenesis. This topic can be explored through interpreting the seismic data. The velocity structure of the Puerto Rico Island and the adjacent Caribbean region has been investigated based on different techniques (e.g., Fischer and McCann, 1984; McCann, 2007; Mendoza and McCann, 2009; Huerfano *et al.*, 2010; Martinez Torres and López Venegas, 2012). The earthquake distributions have also been examined by many researchers (e.g., Asencio, 1980; McCann, 2006, 2007). In our study, cross sections of both the velocity model and seismicity (Figs. 5 and 6) show northward-dipping structures, mainly represented as low-V_P and low-V_P/V_S anomalies. The relocated seismicity shows secondary, gentle northward-dipping planes (~17°) at both shallow (~4 km) and greater (from 10 to 18 km) depths, consistent with the inferred dip angle of the Muertos trough. These results echo previous studies correlating similar dipping features with the hypothesized active subduction (e.g., Mendoza and Huerfano, 2005). Alternatively, the seismogenesis may have been due to

a possible material contrast between the northwest and southwest of the island in the upper 20 km depth, which can also form a dipping structure from south to north. We detect a large high-V_P anomaly at shallow depths beneath the northern side of the GSPRFZ, where batholith has been found at the surface (Weaver, 1958; Learned et al., 1981; Jolly et al., 1998). This correlation suggests that the high-velocity body could possibly represent the plutonic rocks with great material strength, whereas the materials in the southwest are relatively weak as indicated by our velocity models, which could lead to abundant earthquakes occurring at all depths. The subduction process of the Caribbean plate beneath the island of Puerto Rico is inconclusive from only shallow velocity structures and earthquakes, and investigations of the continuity of the dipping plane to greater depths warrant future studies.

Conclusions

We obtain new 3D V_P and V_P/V_S models for the island of Puerto Rico and relocate earthquakes in the region from May 2017 to April 2021 using the resulting velocity models and waveform cross-correlation data. We find prominent high-V_P and low-V_P/V_S anomalies in the eastern and central province between the GNPRFZ and the GSPRFZ, which likely reflect the Utuado pluton. In the western island, the V_P model shows low anomalies beneath both the GSPRFZ and the SLF, which form northerly dipping structures from the southwest to the northwest of the island. The relocated earthquakes have a broad spatial spread, although showing dipping trends along the Investigator fault, the Ponce faults, the Guayanilla rift, and the Punta Montalva fault. The majority of the 2019–2021 Southwestern Puerto Rico earthquakes seem to associate with the Punta Montalva fault. However, more than one fault plane is suggested by the earthquake depth distribution. There is a 17° dipping seismicity trend at various depths, possibly related to the Muertos trough, along which the Caribbean plate is being subducted beneath the Puerto Rico microplate. Our tomographic and relocation results show an active fault network with multiple distinct fault planes, suggesting that regional deformation is accommodated by a diffuse fault structure within a low-velocity zone. The processing of the seismic data collected from a rapid-response seismic reflection survey in March 2020 has already identified numerous faults in the area of the 2019–2021 sequence. Integration with other geophysical and geological data will be valuable for better understanding of the seismic and tectonic activity in the area.

Data and Resources

The seismic data in this study are obtained from the Puerto Rico seismic network (PRSN). The initial earthquake catalog and phase arrivals are available from the PRSN website (http://redsismica.uprm.edu/english/, last accessed May 2021) and are also accessible through the COMCAT catalog maintained by the National Earthquake Information Center (NEIC). The waveforms from all the PRSN stations are stored with the Incorporated Research Institutions for Seismology Data Management Center (IRIS-DMC, http://ds.iris.edu/ds/nodes/dmc/, last accessed May 2021). The 2019 Census data for Puerto Rico was obtained from https://www.census.gov/quickfacts/PR (last accessed May 2021). The maps are created by using the public domain Generic Mapping Tools (GMT; Wessel et al., 2013) and the Matlab available at www.mathworks.com/products/matlab (last accessed October 2021). The supplemental material for this article includes results for the tomographic checkerboard tests, comparison of different location catalogs along one more profile, and the seismicity rate from May 2017 to April 2021 in the study area.

Declaration of Competing Interests

The authors declare that there are no competing interests.

References

Adames-Corraliza, Á. R. (2017). Geomorphic and geophysical characterization of the north Boqueron Bay-Punta Montalva fault zone: A capable fault system in southwestern Puerto Rico, *M.Sc. Thesis*, Department of Geology, University of Puerto Rico, Mayagüez, Puerto Rico.

Addarich-Martínez, L. (2009). The geologic mapping and history of the Guánica Quadrangle, southwestern Puerto Rico, *M.Sc. Thesis*, Department of Geology, University of Puerto Rico, Mayagüez, Puerto Rico.

Asencio, E. (1980). Western Puerto Rico seismicity, *U.S. Geol. Surv. Open-File Rept. 80-192*, 135 pp.

Bachura, M., and T. Fischer (2019). Waveform cross-correlation for differential time measurement: Bias and limitations, *Seismol. Res. Lett.* doi: 10.1785/0220190096.

Bruna, J. G., A. Muñoz-Martín, U. S. Ten Brink, A. Carbó-Gorosabel, P. L. Estrada, J. M. Dávila, and M. C. Morollón (2010). Gravity modeling of the Muertos trough and tectonic implications (north-eastern Caribbean), *Mar. Geophys. Res.* **31,** no. 4, 263–283.

Byrne, D., G. Suarez, and W. McCann (1985). Muertos trough subduction microplate tectonics in the northern Caribbean? *Nature* **317,** no. 6036, 420–421.

Clinton, J. F., G. Cua, V. Huerfano, C. G. von Hillebrandt-Andrade, and J. M. Cruzado (2006). The current state of seismic monitoring in Puerto Rico, *Seismol. Res. Lett.* **77,** no. 5, 532–543.

Corbeau, J., F. Rolandone, S. Leroy, K. Guerrier, D. Keir, G. Stuart, et al. (2017). Crustal structure of western Hispaniola (Haiti) from a teleseismic receiver function study, *Tectonophysics* **709,** 9–19, doi: 10.1016/j.tecto.2017.04.029.

DeMets, C., P. E. Jansma, G. S. Mattioli, T. H. Dixon, F. Farina, R. Bilham, E. Calais, and P. Mann (2000). GPS geodetic constraints on Caribbean–North America plate motion, *Geophys. Res. Lett.* **27,** no. 3, 437–440.

Doser, D. I., C. M. Rodriguez, and C. Flores (2005). Historical earthquakes of the Puerto Rico–Virgin Islands region (1915–1963), in *Active Tectonics and Seismic Hazards of Puerto Rico, the Virgin Islands, and Offshore Areas,* P. Mann (Editor), Geological Society of America Special Paper 385, 103–114.

Eberhart-Phillips, D. (1986). Three-dimensional velocity structure in the northern California Coast Ranges from inversion of local earthquake arrival times, *Bull. Seismol. Soc. Am.* **76,** no. 4, 1025–1052.

Eberhart-Phillips, D. (1990). Three-dimensional P and S velocity structure in the Coalinga region, California, *J. Geophys. Res.* **95,** 15,343–15,363.

Eberhart-Phillips, D. (1993). Local earthquake tomography: Earthquake source regions, in *Seismic Tomography: Theory and Practice,* H. M. Iyer and K. Hirahara (Editors), Chapman and Hall, London, United Kingdom, 613–643.

Efron, B., and R. Tibshirani (1991). Statistical data analysis in the computer age, *Science* **253,** no. 5018, 390–395.

Fischer, K. M., and W. R. Mccann (1984). Velocity modeling and earthquake relocation in the northeast Caribbean, *Bull. Seismol. Soc. Am.* **74,** no. 4, 1249–1262.

Grindlay, N. R., L. J. Abrams, L. Del Greco, and P. Mann (2005). Toward an integrated understanding of Holocene fault activity in western Puerto Rico: Constraints from high-resolution seismic and sidescan sonar data, in *Active Tectonics and Seismic Hazards of Puerto Rico, the Virgin Islands, and Offshore Areas,* P. Mann (Editor), Geological Society of America Special Paper 385, 139–160.

Huerfano, V., C. V. Hillebrandt-Andrade, and G. Bez-Sanchez (2005). Microseismic activity reveals two stress regimes in southwestern Puerto Rico, in *Active Tectonics and Seismic Hazards of Puerto Rico, the Virgin Islands, and Offshore Areas,* P. Mann (Editor), Geological Society of America Special Paper 385, 81–101.

Huerfano, V., A. López Venegas, L. Castillo, G. Báez-Sánchez, L. Soto-Cordero, G. Lin, and Q. Zhang (2010). Improving three dimensional velocity model for Puerto Rico-Virgin Islands for rapid earthquake relocations, *AGU Fall Meeting Abstracts,* San Francisco, California, 13–17 December 2010.

Jansma, P., and G. Mattioli (2005). GPS Results, from Puerto Rico and the Virgin Islands: Constraints on tectonics setting and rates of active faulting, in *Active tectonics and Seismic Hazards of Puerto Rico, the Virgin Islands, and Offshore Areas,* P. Mann (Editor), Geological Society of America Special Paper 385, 13–30.

Jolly, W., E. Lidiak, J. Schellekens, H. Santos, E. Lidiak, and D. Larue (1998). Volcanism, tectonics, and stratigraphic correlations, in *Tectonics and Geochemistry of the Northeastern Caribbean,* Lidiak, E. G., and D. K. Larue (Editors), Geological Society of America Special Paper 322, Boulder, Colorado, 1–34.

Kisslinger, C., and E. R. Engdahl (1973). The interpretation of the Wadati diagram with relaxed assumptions, *Bull. Seismol. Soc. Am.* **63,** no. 5, 1723–1736.

Kumar, S., M. Agrawal, J. Pulliam, E. P. Rivera, and V. A. Huérfano (2020). Crustal thickness and bulk Poisson ratios in the Dominican Republic from receiver function analysis, *Tectonophysics* **775,** 22,8308, doi: 10.1016/j.tecto.2019.228308.

LaForge, R. C., W. R. McCann, and P. Mann (2005). A seismic source model for Puerto Rico, for use in probabilistic ground motion hazard analyses, in *Active Tectonics and Seismic Hazards of Puerto Rico, the Virgin Islands, and Offshore Areas,* P. Mann (Editor), Geological Society of America Special Paper 385, 223–248.

Larue, D. K., R. Torrini, A. L. Smith, J. Joyce, E. G. Lidiak, and D. K. Larue (1998). North Coast Tertiary basin of Puerto Rico: From arc basin to carbonate platform to arc-massif slope, in *Tectonics and Geochemistry of the Northeastern Caribbean,* Lidiak, E. G., and D. K. Larue (Editors), Geological Society of America Special Paper 322, Boulder, Colorado, doi: 10.1130/0-8137-2322-1.155.

Learned, R. E., T. H. Hickey, and I. Perez de Gonzales (1981). A geochemical reconnaissance of the Utuado Batholith and vicinity, Puerto Rico, *U.S. Geol. Surv. Open-File Rept. 81-1131,* doi: 10.3133/ofr811131.

Lin, G. (2018). The source-specific station term and waveform cross-correlation earthquake location package and its applications to California and New Zealand, *Seismol. Res. Lett.* **89,** no. 5, 1877–1885, doi: 10.1785/0220180108.

Lin, G., P. M. Shearer, and E. Hauksson (2007). Applying a three-dimensional velocity model, waveform cross correlation, and cluster analysis to locate Southern California seismicity from 1981 to 2005, *J. Geophys. Res.* **112,** no. B12309, doi: 10.1029/2007JB004986.

Lin, G., and P. G. Okubo (2016). A large refined catalog of earthquake relocations and focal mechanisms for the Island of Hawai'i and its seismotectonic implications, *J. Geophys. Res.* doi: 10.1002/2016JB013042.

Lin, G., and P. G. Okubo (2020). Seismic evidence for a shallow detachment beneath Kilauea's south flank during the 2018 activity, *Geophys. Res. Lett.* **47,** e2020GL088003, doi: 10.1029/2020GL088003.

Lin, G., P. M. Shearer, R. S. Matoza, P. G. Okubo, and F. Amelung (2014). Three-dimensional seismic velocity structure of Mauna Loa and Kilauea volcanoes in Hawaii from local seismic tomography, *J. Geophys. Res.* **119,** no. 5, 4377–4392, doi: 10.1002/2013JB010820.

Lin, G., C. H. Thurber, H. Zhang, E. Hauksson, P. M. Shearer, F. Waldhauser, and J. Hardebeck (2010). A California statewide three-dimensional seismic velocity model from both absolute and differential times, *Bull. Seismol. Soc. Am.* **100,** no. 1, 225–240, doi: 10.1785/0120090028.

Londoño, J. M., K. Vallejo, and S. Quintero (2020). Detailed seismic velocity structure of the Caribbean and Nazca Plates beneath Valle Medio del Magdalena region of NE Colombia, *J. South Am. Earth. Sci.* **103,** 102762, doi: 10.1016/j.jsames.2020.102762.

López Venegas, A., K. Hughes, and E. Vanacore (2020). Puerto Rico's winter 2019–2020 seismic sequence leaves the island on edge, *Temblor* doi: 10.32858/temblor.064.

Mann, P., J.-C. Hippolyte, N. R. Grindlay, and L. J. Abrams (2005). Neotectonics of southern Puerto Rico and its offshore margin, in *Active Tectonics and Seismic Hazards of Puerto Rico, the Virgin Islands, and Offshore Areas,* P. Mann (Editor), Geological Society of America Special Paper 385, 173–214.

Martinez Torres, F., and A. López Venegas (2012). *Using HypoDD and TomoDD to Improve Current Wave Velocity Model in Puerto Rico-Virgin Islands*, COCONet Data and Research Workshop, Tulum, Mexico, doi: 10.13140/2.1.1271.0402.

McCann, W. (2006). Seismotectonics of south and western Puerto Rico: Muer-tos trough downgoing seismic zone and over-riding plate seismicity, *Informe inédito, U.S. Geol. Surv. USGS/NEHRP Final Technical Report: Grant Award Number: 06HQGR0152*.

McCann, W. R. (1985). On the earthquake hazards of Puerto Rico and the Virgin Islands, *Bull. Seismol. Soc. Am.* **75,** no. 1, 251–262.

McCann, W. R. (2007). Improving the seismic hazard model for Puerto Rico: A reliable microearthquake catalog through seismic velocity modeling and microearthquake joint location, *U.S. Geol. Surv. External Res. No. 04HQGR0015*, 1–22.

McCann, W. R., and L. R. Sykes (1984). Subduction of aseismic ridges beneath the Caribbean plate: Implications for the tectonics and seismic potential of the northeastern Caribbean, *J. Geophys. Res.* **89,** no. B6, 4493–4519.

Mendoza, C., and V. Huerfano (2005). Earthquake location accuracy in the Puerto Rico-Virgin Islands region, *Seismol. Res. Lett.* **76,** no. 3, 356–363.

Mendoza, C., and W. McCann (2009). Improving the seismic hazard model for Puerto Rico through seismic tomography and a reliable microearthquake catalog with recalculated magnitudes and calibrated hypocentral error estimates, *U.S. Geol. Surv. External Res. No. 05HQGR0012*, 1–20.

Piety, L. A., J. R. Redwine, S. A. Derouin, C. S. Prentice, K. I. Kelson, R. E. Klinger, and S. Mahan (2018). Holocene surface ruptures on the Salinas Fault and Southeastern Great Southern Puerto Rico fault zone, South Coastal Plain of Puerto Rico, *Bull. Seismol. Soc. Am.* **108,** no. 2, 619–638, doi: 10.1785/0120170182.

Prentice, C., and P. Mann (2005). Paleoseismic study of the South Lajas fault: First documentation of an onshore Holocene fault in Puerto Rico, in *Active Tectonics and Seismic Hazards of Puerto Rico, the Virgin Islands, and Offshore Areas*, P. Mann (Editor), Geological Society of America Special Paper 385, 215–222.

Prentice, C., P. Mann, and G. Burr (2000). Prehistoric earthquakes associated with a late quaternary fault in the Lajas Valley, southwestern Puerto Rico, *Eos Trans. AGU* **81,** F1182.

Roig-Silva, C. M., E. Asencio, and J. Joyce (2013). The northwest trending north Boquerón Bay-Punta Montalva Fault Zone; A through going active fault system in southwestern Puerto Rico, *Seismol. Res. Lett.* **84,** no. 3, 538–550, doi: 10.1785/0220120115.

Schellekens, J. H. (1998). Composition, metamorphic grade, and origin of metabasites in the Bermeja Complex, Puerto Rico, *Int. Geol. Rev.* **40,** no. 8, 722–747, doi: 10.1080/00206819809465234.

Smith, W. H. F., and D. T. Sandwell (1997). Global sea floor topography from satellite altimetry and ship depth soundings. *Science* **277,** doi: 10.1126/science.277.5334.1956.

Symithe, S., E. Calais, J. B. de Chabalier, R. Robertson, and M. Higgins (2015). Current block motions and strain accumulation on active faults in the Caribbean, *J. Geophys. Res.* **120,** no. 5, 3748–3774, doi: 10.1002/2014JB011779.

Thurber, C., and D. Eberhart-Phillips (1999). Local earthquake tomography with flexible gridding, *Comput. Geosci.* **25,** 809–818.

Thurber, C. H. (1983). Earthquake locations and three-dimensional crustal structure in the Coyote Lake area, central California, *J. Geophys. Res.* **88,** no. B10, 8226–8236.

Thurber, C. H. (1993). Local earthquake tomography: Velocities and Vp/Vs-theory, in *Seismic Tomography: Theory and Practice*, Iyer, H. M., and K. Hirahara (Editors), Chapman and Hall, London, United Kingdom, 563–583.

Weaver, J. D. (1958). Utuado pluton, Puerto Rico, *GSA Bull.* **69,** no. 9, 1125–1142, doi: 10.1130/0016-7606(1958)69[1125: UPPR]2.0.CO;2.

Wessel, P., W. H. F. Smith, R. Scharroo, J. Luis, and F. Wobbe (2013). Generic mapping tools: Improved version released, *Eos Trans. AGU* **94,** no. 45, 409–410, doi: 10.1002/2013EO450001.